Remarkable performance of microstructured ceria foams for thermochemical splitting of H2O and CO2 in a novel high–temperature solar reactor

Anita Haeussler, Stéphane Abanades, Anne Julbe, Julien Jouannaux, Martin Drobek, Andre Ayral, Bruno Cartoixa

Remarkable performance of microstructured ceria foams for thermochemical splitting of H_2O and CO_2 in a novel high-temperature solar reactor

Anita HAEUSSLER[1], Stéphane ABANADES[1*], Anne JULBE[2], Julien JOUANNAUX[2], Martin DROBEK[2], André AYRAL[2], Bruno CARTOIXA[3]

[1] Processes, Materials and Solar Energy Laboratory, CNRS-PROMES, 7 Rue du Four Solaire, 66120 Font-Romeu, France

[2] Institut Européen des Membranes, IEM, UMR-5635, ENSCM, CNRS, Univ Montpellier, Place Eugène Bataillon, 34095 Montpellier cedex 5, France

[3] ALSYS-CTI, 382 avenue du Moulinas, 30340 Salindres, France

[*] Corresponding author: Tel +33 (0)4 68 30 77 30

E-mail address: stephane.abanades@promes.cnrs.fr

Abstract

Thermochemical splitting of H_2O and CO_2 applying redox materials constitutes a sustainable option for synthetic fuel production and CO_2 valorization. It consists of two-step process based on the creation of oxygen vacancies in non-stoichiometric oxides during solar-driven thermal reduction, followed by the material re-oxidation with H_2O and/or CO_2 to generate syngas (H_2/CO), the building block for a wide variety of synthetic hydrocarbon fuels. In this work, a monolithic solar reactor was designed and tested integrating reticulated porous ceria (open-cell foams) heated by concentrated solar energy. The influence of various operating parameters on the thermochemical reactor performance was investigated. Increasing the temperature or decreasing the pressure in the reduction step was found to enhance the maximum reduction extent reached by the redox material ($CeO_{2-\delta}$), thereby improving the fuel production capacity. In addition, a decrease of the oxidation temperature led to higher fuel production rate, despite an increase of the temperature swing between the reduction and oxidation steps. Increasing the oxidant concentration also sharply enhanced the oxidation rate. Peak CO production rate approaching 10 mL/min/g was achieved with ceria foams (exhibiting micron-sized grains forming an interconnected macroporous network within the struts) during their reoxidation upon free cooling with pure CO_2 stream (after reduction at

1400°C), thus strongly outperforming (by a factor of about x8) the previous maximum values reported to date. This result was attributed to the fine and stable granular microstructure of the reticulated ceria foams. The solar reactor reliability and robustness during high-temperature two-step redox cycling were demonstrated with an average cycle production of 5.1 mL/g of H_2 and CO, and peak solar-to-fuel efficiencies above 8%. The highly reactive reticulated foams with 10 and 20 ppi (pore per inch) were cycled for about 69 hours (51 cycles) of continuous on-sun operation without any decrease in performance, thus evidencing their noteworthy thermochemical and microstructural stability.

Keywords: solar fuel, solar reactor, ceria foam, reticulated porous ceramic, redox cycle, thermochemical splitting

1. Introduction

Production of synthetic fuels with solar energy is an advantageous solution to replace fossil fuels that increasingly contribute to global warming. Unlike fossil fuel-based energy sources, solar energy is particularly attractive due to its inexhaustibility and its capacity to reduce CO_2 emissions. However, the intermittent aspect of solar energy is of concern for its integration into the current energy market. To solve this issue, solar thermochemical processes represent an efficient route for converting high temperature solar heat into valuable chemical energy carriers (solar fuels). Seasonal solar energy storage via conversion into chemical fuels is therefore possible since such fuels can be used on demand while offering a high energy density. Solar-driven thermochemical cycles for H_2O and CO_2 splitting represent an interesting route to produce syngas that can be further converted to renewable liquid fuels [1]. Indeed, this approach utilizes the entire solar spectrum, thus providing an attractive path to solar fuels production with high energy conversion efficiencies and without any precious metal catalyst. This method can potentially outperform electrolysis because intermediate electricity production is not required. H_2 and CO can be produced by H_2O and CO_2 dissociation, thanks to thermochemical cycles using metal oxide redox pairs as chemical intermediates. H_2 can be used directly as clean energy vector whereas CO/H_2 mixture (syngas) can serve as the building block for the synthesis of various hydrocarbon fuels via the Fischer–Tropsch process [2]. Nowadays, ceria (CeO_2) is considered as the benchmark material to perform two-step thermochemical cycles with stable long-term performance [3–8]. Indeed, ceria is able to maintain its crystallographic structure over a wide range of non-stoichiometry. It provides high oxygen diffusion rates, thermodynamically favorable oxidation with rapid reaction rates, and attractive resistance to sintering. Recently, series of promising

perovskite materials have also been investigated in thermochemical cycles, due to their high non-stoichiometric oxygen exchange capacities and larger reduction extent in comparison with ceria [9–16]. Two-step thermochemical cycles consist of a solar-driven thermal reduction (eq. 1) at high temperature (T_{red} ~1400°C) followed by a re-oxidation step (eq. 2) at lower temperature (T_{ox} ~1000°C) with an oxidizing gas (CO_2 or H_2O). Generic two-step metal oxide thermochemical cycles involving non-stoichiometric oxides are represented by the following reactions:

$$M_xO_y \rightarrow M_xO_{y-\delta} + \frac{\delta}{2}O_2 \quad (1)$$

$$M_xO_{y-\delta} + \delta CO_2(H_2O) \rightarrow M_xO_y + \delta CO(H_2) \quad (2)$$

where δ represents the extent of non-stoichiometry reached by the reactive material. During the thermally-activated reduction step, the oxide is partially reduced leading to the creation of oxygen vacancies and release of O_2. Subsequently, during the oxidation step, the reactive material is re-oxidized, yielding CO or H_2 production [17]. Despite several promising results, the process has not yet been intensively explored, mainly because of low system productivity and/or poor material stability upon cycling. To date, different solar reactor concepts have been investigated for thermochemical cycles. Cho et al. [18,19] performed 13 thermochemical cycles using a 40 kW_{th} solar furnace with CeO_2 reactive coating on inert zirconia foam, yielding an average H_2 production per cycle of about 2.1 mL/g. An isothermal thermochemical cycle was carried out in a 4.4 kW solar reactor using ceria [20], producing 360 mL/min of CO at constant temperature of 1477°C. Using a gas-phase heat recovery system, the solar-to-fuel efficiency reached 1.64 % without taking into account the inert gas energy costs [20]. An electrically-heated monolithic reactor irradiated by artificial light, with porous ceria as reactive material was developed elsewhere [21–23]. Stable and rapid fuel production was demonstrated over 500 cycles with peak and average solar-to-fuel efficiencies of 3.53 % and 1.73 %, respectively [22]. The highest efficiency of ~5% was obtained with T_{red}=1500°C, T_{ox}=800°C and a total pressure of 10 mbar during the reduction step [24]. A counter rotating ring reactor was also designed [25–27], yielding instant solar-to-fuel efficiency of 1.7% and peak CO production rate of 100 mL/min.

A novel 1.5 kW monolithic solar reactor was designed and developed at PROMES laboratory for two-step thermochemical H_2O and CO_2 splitting with non-stoichiometric metal oxides as oxygen carrier redox materials. The ceria material was integrated in the form of reticulated foam inside the reactor cavity. Such a porous structure acting as the reactive material itself inherently combines the advantages of efficient volumetric radiative absorption, low pressure drop, high surface area, rapid reaction rates, and high mass loading of the reactive material.

Low optical thickness (i.e., low opacity) for incident thermal radiation is desired to enable both volumetric radiative absorption and uniform heating of the porous structure. On the other hand, the oxidation step with H_2O or CO_2 is known to be largely surface dependent, and thus a large surface area is required to enhance reaction kinetics. Hence, a trade-off must be found between rapid reaction kinetics and efficient radiation heat transfer, by combining both of the desired properties, namely: low optical thickness for volumetric radiative absorption during reduction and high surface area for rapid reaction rates during oxidation. In addition, low porosity is favorable for high material mass loading in the reactor. The above issues have to be considered when dealing with porous reactive structures. In this respect, the ceria reactant was loaded in the form of reticulated porous foams with both uniform cell size density (millimetric scale) for solar radiation volumetric absorption and granular microstructure (micron-sized grains forming an interconnected macroporous network) within the foam struts for enhanced oxidation reaction. The experimental performance assessment of the reactor has been conducted to determine the most relevant operating parameters encompassing the reactions temperatures, reduction pressure, type and concentration of oxidant, influencing the solar fuel production. Indeed, the identification of suitable operating parameters to reach optimized thermochemical performance is essential for further process scale-up. Specifically, the amounts of produced fuel and fuel production rates have been optimized. Such a detailed parametric optimization carried out on a real solar reactor operated with reticulated porous ceria structures under representative operating conditions has never been achieved to date.

2. Materials and method

The reactive ceria material (99.9% purity) was shaped as reticulated porous foams with a cylindrical geometry, as presented in Figure 1. Ceria foams (CF) with two homogeneous cell size densities were used (10 and 20 pores per inch, ppi), designated in the following as CF-10 (10 ppi) and CF-20 (20 ppi). The center of the foam cylinder was hollow to form a cavity (closed at the bottom by a disc) in order to promote radiative heat transfer and uniform heating along the foam height. Both foams featured ~87% porosity (0.92 g/cm^3 and 0.93 g/cm^3 bulk density for CF-10 and CF-20, respectively, not including the central cavity volume) and were produced according to the well-known process of polymeric sponge replication [28]. First, a selected polymeric and flexible open-celled sponge with defined pore density was immersed in a ceramic slurry containing organic binders. The excess of slurry was then removed by compressing the sponge and a drying step allowed hardening the ceramic-based material. Finally, a few hours thermal treatment in air at 1450°C was applied

to both remove the organics (binders and polymeric sponge), and sinter the foam thereby providing mechanical integrity to the final porous ceramic structure.

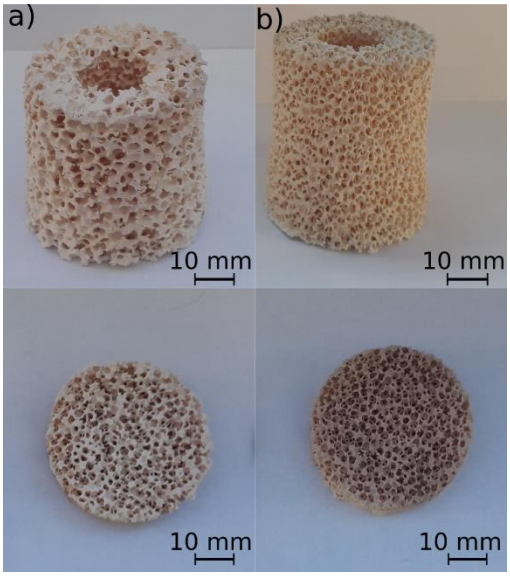

Figure 1: Reticulated porous ceria foams composed of a hollow cylinder and a bottom disc, with a) 10 ppi (cylinder: ~44 mm o.d., 15 mm i.d., 40 mm height; disk: ~43 mm diameter, 10 mm height; total foam mass: 55.7 g) and b) 20 ppi pore density (cylinder: ~39 mm o.d., 15 mm i.d., 44 mm height; disk: ~42 mm diameter, 10 mm height; total foam mass: 55.9 g).

Solar experiments were performed using vertical-axis medium-size solar facilities of PROMES-CNRS laboratory. The solar concentrating system consists of a 2 m-diameter parabolic dish along with a sun-tracking heliostat. The solar monolithic reactor (Figure 2) was designed to perform two-step temperature-swing cycles while alternately switching between inert gas for O_2-releasing reduction and oxidant gas (H_2O or CO_2) for the splitting step. The reaction chamber was composed of an insulated alumina cavity with cylindrical shape (50 mm inner diameter and 80 mm height) and closed by an alumina top cover with 19 mm diameter aperture at the upper front to absorb concentrated solar radiation. A fibrous layer of porous alumino-silicate wrapped the cavity to insulate it (40 mm thickness, density 400 kg/m^3, thermal conductivity 0.14 W/m.K at 800°C). In addition, a zirconia felt (3 mm thick) was used to insulate the front alumina wall of the aperture plate, thereby reducing radiative losses at the upper front. The cavity receiver configuration combined with the small aperture size advantageously led to maximum incident radiation absorption, while re-radiation loss from the cavity to the surrounding environment was minimized. A transparent Pyrex window was hermetically placed on top of the reactor in order to let the concentrated solar flux reach the cavity. The reactor stainless steel shell was water-cooled. The ceria foam (~ 55 g) was

settled within the cavity in which the gas flow was injected from the upper side (both via window and lateral inlets). The gas flow-rates (Ar: 99.999% purity with [O_2] < 2 ppm, and CO_2: 99.995% purity) were controlled and adjusted via mass-flow controllers (MFC, Brooks Instruments model SLA5850S). Ar gas was continually injected via the window to provide inert gas atmosphere. The gas then flowed through the cavity after entering via the aperture. Moreover, the reactive gas was injected from the top lateral side of the cavity below the aperture for rapid switch of gas composition between the reduction and oxidation steps. Pure Ar was injected during the reduction step whereas a mixture of Ar and CO_2 (or steam) was injected during the oxidation step. Water was injected using a liquid mass flow controller (range 0-60 g/h, accuracy ±1% of full scale) via an alumina capillary inside the lateral tube inlet. Water was vaporized when exiting the capillary tube and steam was transported by the Ar carrier gas to the cavity. The reactive gas then flowed through the foam and exited via a single outlet port at the cavity bottom. During the reduction step, Ar (1.2 NL/min) swept the reactor during heating (up to ~1400°C) thanks to the solar energy input controlled by an intermediate shutter placed below the reactor frame. During the heating stage, oxygen concentration in the outlet gas was continuously measured to monitor the progress of the reduction reaction. After complete reduction of the reactive material ascertained by continuous decrease of O_2 concentration, the reactor was cooled down by closing the shutter and removing the solar input. When the oxidation temperature was reached (~1000°C), the oxidant gas (either H_2O or CO_2, at controlled molar fraction) was fed in order to re-oxidize the reactive material. The foam temperature was monitored with two B-type thermocouples (T1 and T2) coupled to a pyrometer (measuring at 4.8-5.2 µm) pointing at the foam center inside the foam cavity (through a CaF_2 window), as shown in Figure 2. T1 was in contact with the ceria foam and vertically positioned at the transition between the cylindrical and disc parts of the foam, whereas T2 was setback at about 1 cm from the foam to avoid direct exposure to solar radiation and overheating. It can be thus assumed that the representative minimum temperature of the foam was given by T1 (placed at the foam bottom) and the average foam cavity temperature was given by the pyrometer. The reactor pressure was measured by pressure transmitters placed at both gas inlets (window and lateral) and cavity. The operating pressure during the reduction step was possibly decreased by using a primary vacuum rotary vane pump at the reactor outlet, in order to study the effect of the total pressure (during reduction step) on both the reduction extent and associated fuel production yield. The pump was thus only used when aiming at decreasing the pressure during reduction. For the oxidation step, the pump was stopped, the pressure was increased again by filling with Ar and then the gas outlet was connected directly to the gas analyzer. In all cases, continuous flowing gas through the foam (with negligible pressure drop) was applied to remove and carry the gas product species to the outlet, thus favouring reactions completion.

The outlet gas flowed through a bubbler to condense and remove excess steam, and a gas dryer (desiccant column) was used to remove residual moisture before gas analysis. In the case of H_2O splitting, the excess water was entirely condensed and trapped and the exit gas stream to be analyzed was thus composed of Ar/H_2 binary mixture. In the case of CO_2 splitting, the outlet gas contained unreacted CO_2 in addition to Ar and CO. The output gas was analyzed online (continuous evolution of concentrations versus time) to determine both the oxygen and fuel (H_2 or CO) production rates at each step. The O_2 concentration in the exhaust was measured by a trace O_2 electrochemical analyzer (Systech, range from 0.1 ppm to 1%, precision ±2% of reading). Both CO and CO_2 concentrations were measured by a NDIR analyzer (MGA3000, scale: 0–30% for CO, 0-100% for CO_2, precision ±1% of full scale). H_2 was analyzed by a catharometer based on thermal conductivity detection (calibrated for Ar/H_2 binary mixture, scale: 0-10%, precision: 1% of full scale). The response time for both H_2 and CO detection after oxidant injection was less than 10 s. Their concentrations reached a maximum just after CO_2 or H_2O injection (peak fuel production rate) and then steadily dropped to zero denoting complete ceria oxidation. The oxidizing gas feed was then stopped and the system was purged with Ar before increasing the temperature again for the next reduction step. An automated acquisition system (Beckhoff) was used for recording the data (i.e. reactor temperatures, pressures, gas flow-rates, and outlet gas concentrations with a time step of 1 s). The gas production yields (O_2 and H_2 or CO) were calculated by time integration of the gas production rates over the duration of the reduction and oxidation steps (with a relative uncertainty of ±2%).

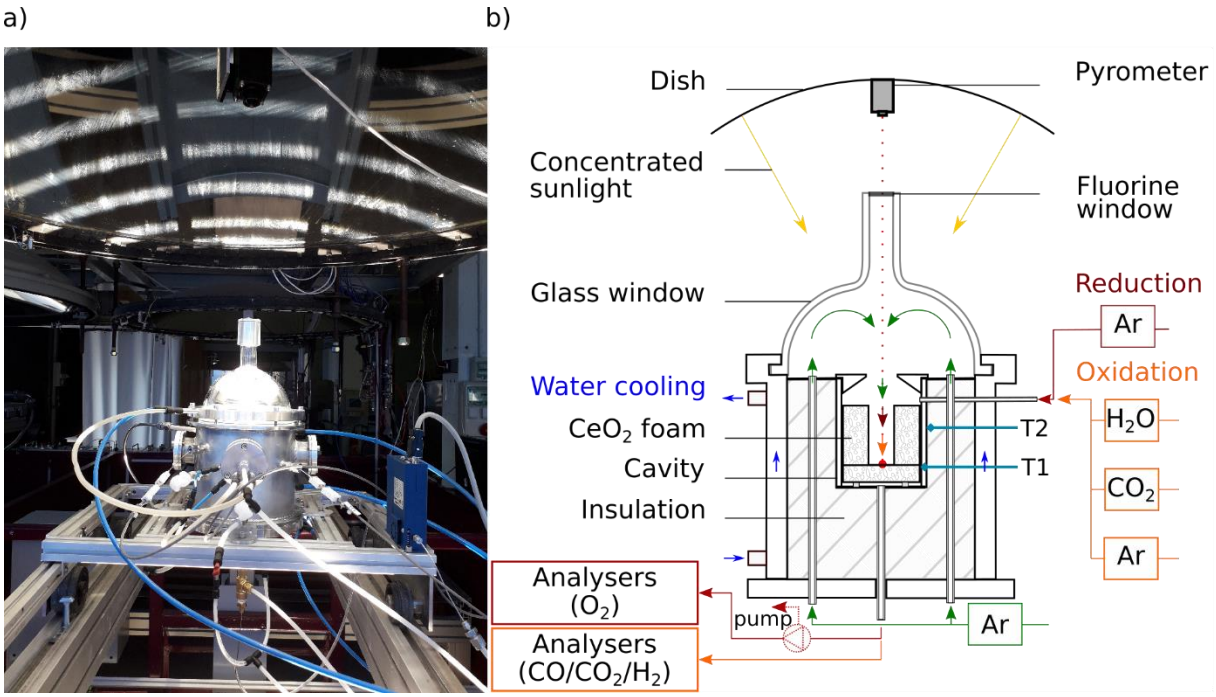

Figure 2: a) Photo of the experimental set-up during on-sun operation and b) scheme of the SUNFUEL solar reactor enabling two-step thermochemical cycles with reticulated porous ceria foams for H_2O or CO_2 splitting.

3. Results and discussion

The influence of operating parameters on the solar fuel production was investigated. Unravelling their influence on fuel production was required to optimize the process performance and to determine the solar-to-fuel energy conversion efficiency. In such two-step process, the parameters of both the reduction and oxidation steps need to be varied separately to determine their impact on fuel production. The detailed lists of the operating parameters for each cycle performed with the different ceria foams (CF-10 and CF-20) are given in Table 1. The CF-10 foam underwent 37 cycles, yielding a total production of 8.97 NL of CO (34 cycles) and 0.68 NL of H_2 (3 cycles). Likewise, the CF-20 foam was submitted to 14 cycles and produced 1.10 NL of H_2 (4 cycles) and 2.78 NL of CO (10 cycles). In total, the CF-10 and CF-20 foams sustained 51 h and 18 h of continuous on-sun operation, respectively, with no apparent performance decline.

Table 1: Operational parameters and fuel production performance for the CF-10 and CF-20 foams (T_{red} is the reduction temperature, P_{red} the reduction pressure and T_{ox} the oxidation temperature; gas flow-rates are given at normal conditions).

Cycle #	Reduction step parameters				Oxidation step parameters						
	T_{red} (°C)	P_{red} (hPa)	Ar flow rate during reduction (L/min)	O_2 produced (µmol/g)	Oxidant gas	Oxidation temperature regime	T_{ox} (°C)	Oxidant gas molar fraction	Oxidant gas flow rate (total flow rate) (L/min)	Fuel produced (µmol/g)	Peak fuel production rate (mL/g/min)
CF-10 foam											
1	1378	870	1.2	105	H_2O	Isothermal	967	0.17	0.25 (1.45)	208	0.57
2	1417	870	1.2	109	H_2O	Isothermal	1006	0.17	0.25 (1.45)	216	0.76
3	1404	870	1.2	106	CO_2	Isothermal	1034	0.25	0.40 (1.60)	213	1.43
4	1407	880	1.2	97	CO_2	Isothermal	1032	0.25	0.40 (1.60)	188	1.32
5	1400	872	1.2	107	CO_2	Isothermal	1079	0.25	0.40 (1.60)	212	1.10
6	1412	868	1.2	88	CO_2	Isothermal	1114	0.25	0.40 (1.60)	120	0.59
7	1407	866	1.2	84	CO_2	Isothermal	1121	0.25	0.40 (1.60)	161	0.53
8	1380	170	1.2	102	CO_2	Isothermal	907	0.25	0.40 (1.60)	203	1.61
9	1408	870	1.2	88	CO_2	Isothermal	1213	0.25	0.40 (1.60)	136	0.48
10	1408	879	1.2	98	CO_2	Isothermal	1059	0.25	0.40 (1.60)	194	0.81
11	1453	870	1.2	116	CO_2	Isothermal	1050	0.25	0.40 (1.60)	226	1.18
12	1404	876	1.2	98	CO_2	Isothermal	869	0.25	0.40 (1.60)	197	3.49
13	1403	872	1.2	78	CO_2	Isothermal	1011	0.25	0.40 (1.60)	151	0.91
14	1405	880	1.2	86	CO_2	Isothermal	1055	0.25	0.40 (1.60)	152	1.00
15	1402	885	1.2	96	CO_2	Isothermal	954	0.25	0.40 (1.60)	191	2.69
16	1458	878	1.2	119	CO_2	Isothermal	1061	0.25	0.40 (1.60)	237	1.40
17	1405	875	1.2	77	H_2O	Isothermal	1057	0.17	0.25 (1.45)	129	0.12
18	1407	851	1.2	110	CO_2	Dynamic	1020-904	0.25	0.40 (1.60)	241	2.31
19	1227	872	1.2	39	CO_2	Dynamic	998-764	0.25	0.40 (1.60)	82	1.23
20	1413	866	1.2	116	CO_2	Dynamic	1062-828	0.25	0.40 (1.60)	250	1.95
21	1410	863	1.5	125	CO_2	Dynamic	1005-799	0.25	0.40 (1.60)	254	2.48
22	1401	863	1.5	102	CO_2	Dynamic	1042-833	0.25	0.40 (1.60)	208	2.29
23	1240	870	2.0	58	CO_2	Dynamic	1185-724	0.29	0.40 (1.40)	115	0.43
24	1408	869	2.0	123	CO_2	Dynamic	988-850	0.50	1.00 (2.00)	250	6.25

25	1410	862	2.0	110	CO_2	Dynamic	993-836	0.50	1.00 (2.00)	217	5.41
26	1407	862	1.2	114	CO_2	Dynamic	1008-796	1.00	2.00 (2.00)	254	8.36
27	1407	861	1.2	108	CO_2	Dynamic	1018-791	1.00	2.00 (2.00)	237	7.27
28	1403	861	1.2	120	CO_2	Dynamic	1007-797	1.00	2.00 (2.00)	252	9.43
29	1402	859	1.2	104	CO_2	Dynamic	1014-770	1.00	2.00 (2.00)	201	8.08
30	1401	858	1.2	90	CO_2	Dynamic	1010-839	0.25	0.40 (1.60)	160	2.09
31	1405	106	1.2	128	CO_2	Dynamic	1001-772	0.25	0.40 (1.60)	258	2.57
32	1403	110	1.2	141	CO_2	Dynamic	986-825	0.67	2.00 (3.00)	283	9.93
33	1409	116	1.2	130	CO_2	Dynamic	1020-752	0.50	1.00 (2.00)	262	4.51
34	1403	116	1.2	127	CO_2	Dynamic	1010-834	0.50	1.00 (2.00)	241	5.22
35	1401	114	1.2	141	CO_2	Dynamic	1015-775	1.00	2.00 (2.00)	284	7.55
36	1402	116	1.2	142	CO_2	Dynamic	1013-744	1.00	2.00 (2.00)	282	7.47
37	1328	92	0.8	85	CO_2	Dynamic	1002-812	0.50	1.00 (2.00)	171	3.55
CF-20 foam											
1	1410	876	1.2	110	CO_2	Isothermal	1064	0.25	0.40 (1.60)	186	1.10
2	1408	877	1.2	67	CO_2	Isothermal	1162	0.25	0.40 (1.60)	81	0.34
3	1411	879	1.2	60	CO_2	Isothermal	1056	0.25	0.40 (1.60)	121	0.89
4	1409	872	1.2	87	CO_2	Isothermal	955	0.25	0.40 (1.60)	197	2.05
5	1412	876	1.2	95	H_2O	Isothermal	1053	0.17	0.25 (1.45)	118	0.30
6	1401	910	1.2	90	H_2O	Isothermal	870	0.17	0.25 (1.45)	250	1.20
7	1410	870	1.2	106	CO_2	Isothermal	903	0.25	0.40 (1.60)	210	3.38
8	1410	874	1.2	118	CO_2	Isothermal	705	0.25	0.40 (1.60)	273	5.02
9	1424	110	1.2	174	CO_2	Isothermal	1048	0.25	0.40 (1.60)	296	1.68
10	1407	878	1.2	108	H_2O	Isothermal	858	0.17	0.25 (1.45)	222	0.83
11	1409	872	1.2	123	CO_2	Dynamic	1016-893	0.25	0.40 (1.60)	261	2.67
12	1407	869	1.2	126	CO_2	Dynamic	996-847	0.25	0.40 (1.60)	260	2.69
13	1456	872	1.2	149	CO_2	Dynamic	997-845	0.25	0.40 (1.60)	301	3.33
14	1454	870	1.2	135	CO_2	Dynamic	1004-673	0.25	0.40 (1.60)	266	1.34

3.1. Parameters investigated during the reduction step

According to thermodynamics, the oxygen partial pressure and the reduction temperature are the key parameters determining the maximum reachable oxygen non-stoichiometry in the ceria structure [29,30]. In order to study the influence of oxygen partial pressure, a vacuum pump was placed at the reactor output to lower the total operating pressure by about one order of magnitude compared with atmospheric pressure. The total inert gas flow was kept unchanged, in order to assess only the effect of the total pressure. The minimum pressure achievable with flowing gas (~100 hPa) is still reasonable and easily accessible in large-scale processes. Further decreasing the pressure would bring additional energy penalty (pumping work) and thus cannot be considered when aiming the development of a scalable process. Figure 3a depicts the evolution of the oxygen non-stoichiometry *versus* temperature while heating the reactor at two different pressures during the reduction step. The temperature increase leads to the rise of oxygen non-stoichiometry for both pressures. Decreasing the pressure significantly increases the maximum non-stoichiometry reached by the reactive material at the final reduction temperature T1=1400°C (δ=0.044 at 106 hPa versus 0.031 at 865 hPa). Furthermore, the onset temperature decreases by ~350°C when decreasing the pressure from 865 hPa to 106 hPa. Figure 3b shows the O_2 and CO amounts produced for the two cycles performed at the different pressures during reduction. Decreasing the pressure during the reduction step significantly increases the produced oxygen amount (90 µmol/g to 128 µmol/g), which subsequently enhances CO production during the oxidation step. For a pressure of 106 hPa during the reduction step, a ceria reduction extent δ/δ_{max}=8.8% is reached at T1=1400°C (δ_{max}=0.5 for complete reduction of Ce^{4+} to Ce^{3+}). This high reduction extent then boosts the amount of fuel produced during the oxidation step (from 160 µmol/g to 258 µmol/g). Moreover, the cycle performed at low pressure in Figure 3 shows a total CO_2 conversion extent of 7.5% and a CO_2 conversion peak of 36% measured at the peak rate of CO production (in comparison with 6.3% and 29%, respectively, for the cycle at atmospheric pressure). A reduced oxygen partial pressure thus shows a beneficial impact on both the reduction extent and fuel production yield achievable by the reactive ceria material.

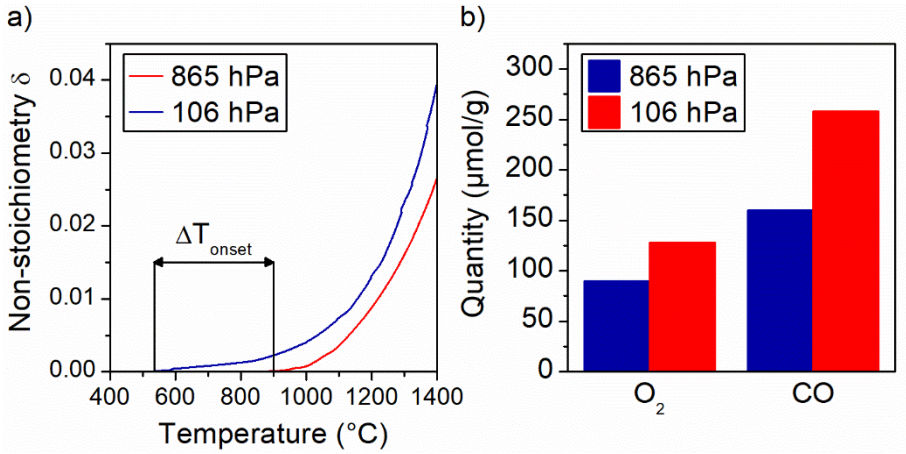

Figure 3: Investigation of CF-10 foam performance in the solar reactor (cycles #30 and #31). a) Evolution of non-stoichiometry as a function of temperature for two different operating pressures and b) amounts of O_2 and CO produced for different reduction pressures.

The reduction temperature is the other key parameter affecting the thermochemical cycle performance. Figure 4 illustrates the O_2 and CO production rates evolution for two cycles carried out at different reduction temperatures (1400 vs. 1450°C, T1 was selected as the reference temperature measurement). Increasing the reduction temperature by 50°C leads to an increase of the O_2 production from 126 µmol/g to 149 µmol/g. The reduction extent reached with a reduction temperature of 1450°C is about δ=0.051 (at atmospheric pressure). As a result of the reduction extent being increased when the temperature increases, the amount of CO produced is also increased (from 260 µmol/g at 1400°C up to 301 µmol/g at 1450°C). Furthermore, the CO_2 conversion is increased from 8.7% to 10.9% together with the peak CO_2 conversion (from 38% to 47%). The increase of the reduction temperature thus shows a beneficial impact on the production of both O_2 and CO. Of course, such temperature increase must be limited due to the risk of the redox material sublimation and fastened ageing that may cause performance loss [7, 22]. Thus, the maximum temperature was kept at 1450°C (measured by T1 thermocouple), while admitting that higher temperatures are reached in the upper part of the foam exposed to high-flux radiation (as evidenced by the higher temperature values, ~30-50°C, measured by the pyrometer in the central foam cavity). Moreover, the increase of the reduction temperature implies an increase of the heat loss due to the increase of the temperature swing (ΔT) between redox cycle steps.

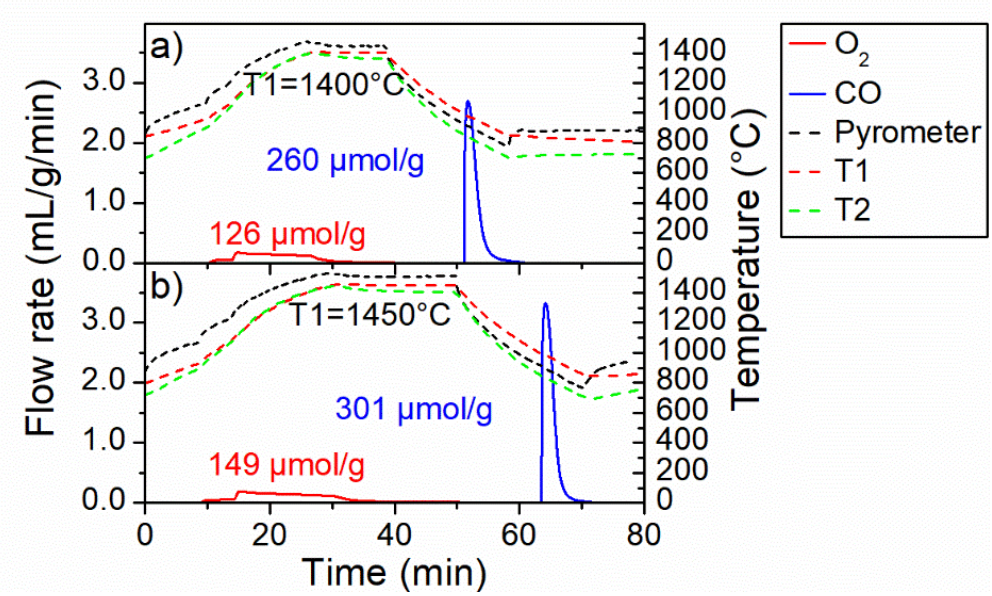

Figure 4: Evolution of O_2 and CO production rates along with the temperatures for two thermochemical cycles with reduction performed at a) 1400°C (cycle #12) and b) 1450°C (cycle #13) at atmospheric pressure for CF-20 foam.

The argon flow also impacts the oxygen partial pressure by diluting the O_2 released by ceria during the reduction step. As confirmed previously, the total pressure affects the oxygen partial pressure and sharply influences the ceria reduction extent. Varying the argon flow-rate is another way to tune the oxygen partial pressure. This parameter has thus been investigated to demonstrate its influence on the reduction step. Figure 5 shows the evolution of O_2 amount produced according to the argon flow-rate during the reduction step. An increasing argon flow lowers the oxygen partial pressure, which thereby significantly favors the reduction extent. This result can be explained by a higher dilution of the oxygen released during the reduction step (lower oxygen partial pressure). Indeed, increasing the argon flow-rate from 1.2 L/min to 2 L/min moderately increases the oxygen production yield from 99 to 117 µmol/g whereas the CO yield increases from 198 to 234 µmol/g. In comparison with the decrease of the total pressure, increasing the argon flow rate enhances the oxygen yield by 17%, whereas a pressure decrease from 865 hPa to 106 hPa improves the oxygen yield by 42%. This can be explained by a difference in oxygen partial pressure, which decreases only twice when doubling the Ar flow whereas it drops ~8 times when decreasing the total pressure from 865 to 106 hPa. Thus, the Ar flow rate would need to be dramatically increased to obtain the same effect as the total pressure reduction, which would cause considerable heat loss together with high inert gas consumption. Therefore, decreasing the total pressure during the reduction step is more relevant than increasing the carrier gas flow-rate.

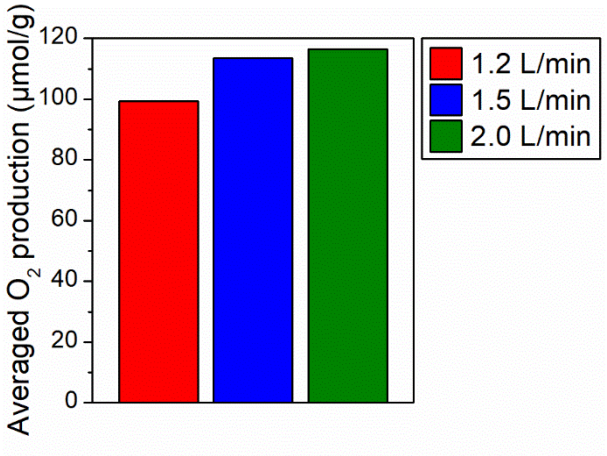

Figure 5: Influence of the argon flow-rate on the average oxygen production for CF-10 foam (T_{red}~1400°C, atmospheric pressure).

In summary, a reduction step at low pressure and high temperature is favorable to enhance fuel production yield. In contrast, the argon flow-rate does not impact significantly on the reduction step in comparison with total pressure reduction. In addition, significantly higher inert gas flow-rate would be required to obtain equivalent impact as total pressure reduction, although it is not realistic for process upscaling.

3.2. Parameters investigated during the oxidation step

The oxidation step was performed by adding the oxidant gas in the feed via the lateral gas inlet located above the ceria foam. Kinetics of CO_2 reduction over nonstoichimetric ceria has been investigated [31]. The CO_2 molar fraction (x_{CO_2}) injected in the reactor during the oxidation step is a key parameter mastering the fuel production rate. In order to highlight the influence of this parameter on CO production rate, three thermochemical cycles have been performed with the same reduction temperature (T1=1400°C) and different CO_2 molar fractions (25%, 50% and 100%) during the oxidation step. The results are presented in Figure 6a (for the oxidation test with pure CO_2, the argon flow usually injected in the window zone was replaced by CO_2). Increasing the CO_2 concentration results in a sharp increase of CO production rate, while the oxidation duration is concomitantly reduced (from 3.8 min to 1.7 min to obtain 90% of the maximum CO amount produced). The maximum CO production rate reached ~9.4 mL/g/min for oxidation in 100% CO_2 (cycle #28 in Table 1). This means that a 8 fold-increase of the fuel production rate was achieved with the studied micro-structured ceria foams (microstructural characterization provided in the next section), when compared to previously reported values [18,23,24,32]. The fuel production rate can even be enhanced further (up to 9.9 mL/g/min for cycle #32) by increasing the total gas flow-rate

(inducing products dilution). The peak of CO_2 to CO conversion reached 21%, 25% and 36% whereas the global CO_2 to CO conversion over the oxidation step duration reached 1.6%, 2.1% and 7.4% for CO_2 molar fractions of 1.00, 0.50 and 0.25, respectively. Furthermore, the produced CO amounts were similar regardless of the CO_2 molar fraction (in the range of 258-284 µmol/g), which denotes complete ceria oxidation even though the kinetics is strongly dependent on the oxidant gas concentration. This result also means that the conversion of pure CO_2 streams (e.g. issued from post-combustion CO_2 capture processes) is particularly attractive to favor reaction kinetics. Increasing the CO_2 molar fraction increases the driving force of surface oxidation reaction (by increasing the amount of CO_2 available at the surface) and further promotes oxygen diffusion within ceria thanks to the gradient of oxygen concentration. In addition, it also decreases the $CO:CO_2$ ratio as shown in Figure 6b, which thermodynamically favors the oxidation step. In other words, larger CO_2 concentration favors the thermodynamic equilibrium towards CO production. However, considering an industrial process, a lower $CO:CO_2$ ratio will require higher amount of supplementary energy to separate CO from CO_2. In summary, a high CO_2 molar fraction in the oxidation step promotes kinetics, which leads to a fast (short-time duration) oxidation reaction, but at the expense of lower CO_2 to CO conversion extent.

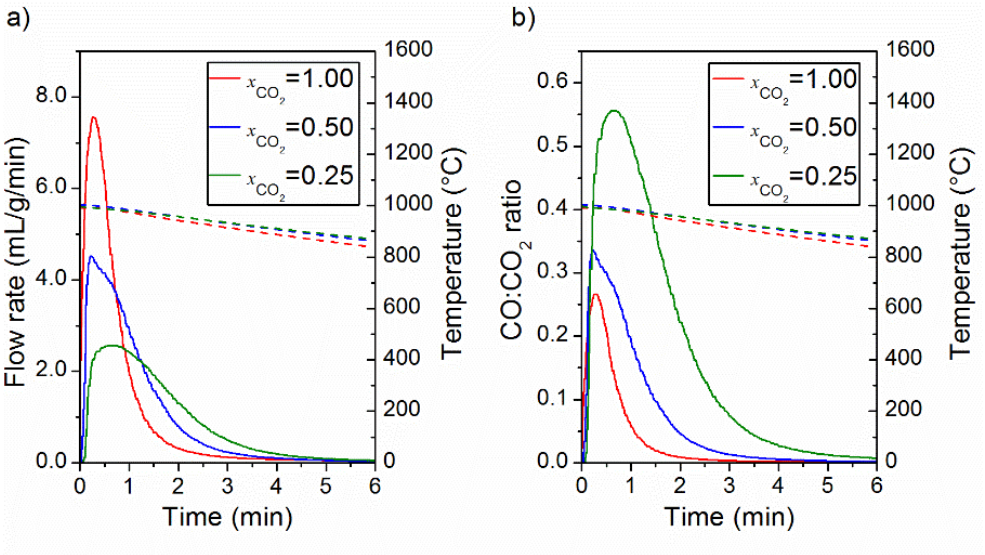

Figure 6: Evolution of a) CO production rates (solid lines) and b) CO to CO_2 ratio (solid lines) for different inlet CO_2 molar fractions (0.25, 0.50 and 1.00) along with T1 temperatures (dashed lines), during cycles #31, #33 and #35 with CF-10 foam, respectively.

The temperature plays a major role in the oxidation step performance. To study its influence on the fuel production, three thermochemical cycles were carried out at different oxidation temperatures (T1=1150, 1050 and 950°C), as shown in Figure 7a. The lower the oxidation temperature, the higher the amount of CO produced. For instance, CO production increases

from 81 µmol/g to 197 µmol/g when the oxidation temperature decreases from 1150°C to 950°C. Furthermore, the CO peak production rate at 950°C roughly increases by a factor x5 when compared with an oxidation performed at 1150°C. Therefore, decreasing the oxidation temperature leads to fuel production enhancement by improving both the production rate and the fuel yield. On the other hand, decreasing the oxidation temperature increases the temperature swing (ΔT) between the reduction and oxidation steps, which induces sensible heat losses. This basically explains why isothermal or near-isothermal cycling has been commonly proposed based on theoretical efficiency calculations when kinetic aspects are not addressed [33-34], despite other studies pointed out the lowest efficiencies for isothermal operation [35-36]. Anyway, the strong effect of oxidation temperature on kinetics suggests that low temperature swing is definitely not appropriate to operate such redox cycle as the oxidation kinetics would be too slow and thus extend tremendously the reaction duration, which is unsuitable in practice. Conversely, high temperature swing inducing heat losses is often associated with a requirement for sensible heat recovery system, and the benefits of heat-recovery strategies on system efficiency [37], especially solid heat recuperation for lower oxidation temperatures have been shown in thermodynamic analyses [38]. However, solar energy is freely available and decreasing the amount of solar energy between steps has in reality no impact on the global cycle performance, because it does not change the size/cost of the solar concentrating system which is primarily required for the reduction step only. Therefore, the sole parameter of importance being cycle duration, the reaction kinetics should be favored in priority as it mostly influences the amount of fuel produced during a working day. The global kinetic rate of the two-step process that determines the cycle duration thus mainly depends on both the heating rate (determining the rate of reduction step) and the oxidation rate (favored by low temperature and high oxidant concentration).

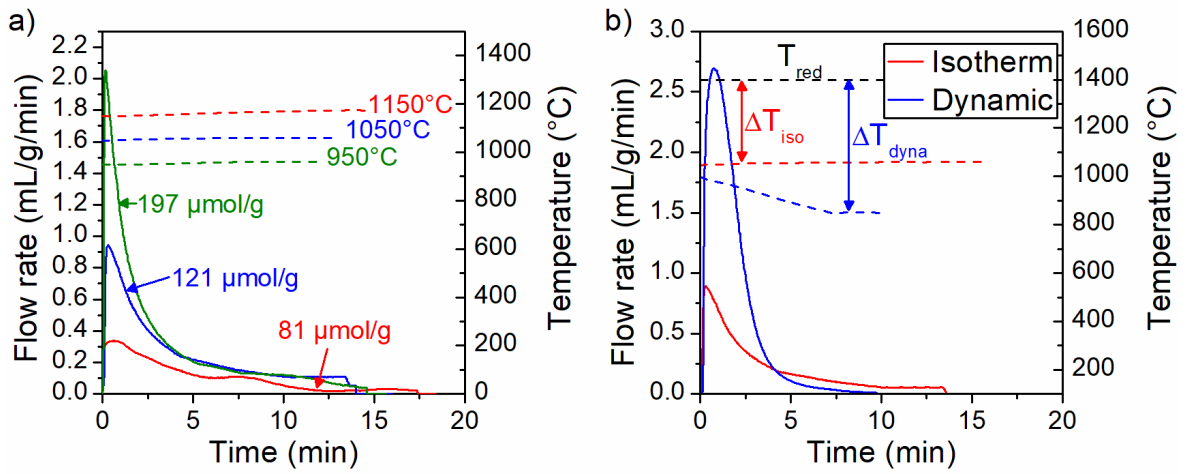

Figure 7: Evolution of CO production rate (solid lines) for (a) different oxidation temperatures T1 (dashed lines) in isothermal regime, during cycles #2, #3 and #4 with CF-20 foam, and (b) isothermal and dynamic oxidation temperature regimes along with temperature T1 (dashed lines), for cycles #3 and #12 with CF-20 foam, respectively.

During the oxidation step, two temperature regimes were considered (isothermal and dynamic). The former consists of an oxidation at constant temperature maintained by solar energy input, whereas the latter proceeds with an oxidation during free cooling without any energy input. Figure 7b compares the CO production rate using either isothermal or dynamic regime. The maximal production rate in isothermal condition (at 1050°C) is lower than in dynamic conditions. Moreover, the CO production in the dynamic regime occurs on shorter duration when compared with the isothermal one (CO_2 injection was started at ~1000°C and stopped at ~850°C). This is due to the higher oxidation temperatures (thermodynamically unfavorable) for the isothermal condition. In contrast, the constant temperature decrease during dynamic oxidation raises the thermodynamic driving force of the oxidation reaction. Moreover, the CO production yield during dynamic oxidation (260 µmol/g) is higher than under isothermal conditions (121 µmol/g). The fuel production is thus favored by the dynamic free cooling temperature regime. However, the temperature swing (ΔT) is higher with the dynamic regime, which induces sensible heat losses.

Both CO_2 and H_2O have been considered as oxidant gases for fuel production. Figure 8 compares H_2 and CO production rates in isothermal conditions at 900°C and 1050°C (after a reduction step at T1=1400°C). A decrease of the oxidation temperature enhances markedly the fuel production rate for both CO_2 and H_2O. Regardless of the oxidation temperature, the peak production rate of CO is higher than the H_2 one. Considering thermodynamics, this

phenomenon can be attributed to more favorable CO_2 dissociation than H_2O dissociation. The output gas is a mixture of unconverted reactant and products that would require further separation step. While H_2 separation from H_2O is straightforward by steam condensation, CO removal from CO_2 requires additional energy and/or advanced separation technology.

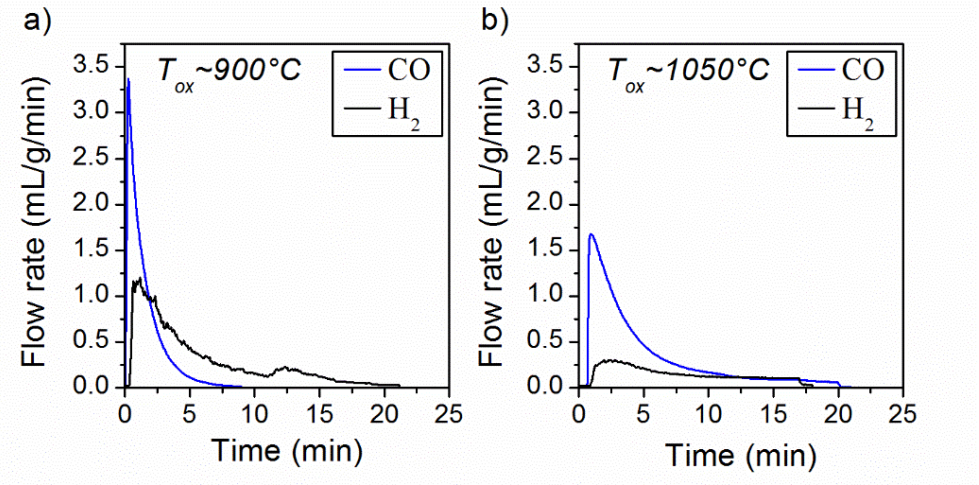

Figure 8: Evolution of H_2 and CO production rates with an oxidation temperature of a) 900°C (cycles #6 and #7 of CF-20) and b) 1050°C (cycles #5 and #9 of CF-20).

3.3. Thermal stability of the porous ceria foams

Considering that industrial processes require reactive materials withstanding multiple cycles without any performance decline, consecutive cycles have been performed with both CF-10 and CF-20 foams. Due to solar energy variability in a real solar process, the material cannot be subjected to strictly identical parameters from cycles to cycles, and it will thus have to sustain multiple changes in the cycling conditions, thereby favoring process flexibility. Typical results are shown in Figure 9 for CF-20 foam tested with the reduction steps carried out at ~1400°C and 110 hPa, and oxidation steps from 1000°C to 750°C (dynamic conditions with CO_2 molar fraction of 0.5 for cycles #33 and #34, and 1.0 for cycles #35 and #36). Noticeably, repeatable results were obtained when using similar operational conditions. Furthermore, the CO production rate was remarkably high, in the range of 4 to 7 mL/g/min, representing the highest rates obtained to date with ceria and thus a strong improvement in the performance of solar fuel reactors based on reticulated porous ceria. In comparison, Furler et al. [23,24,32] obtained a maximal fuel production rate of 1.2 mL/g/min with more stringent operational conditions (1450°C and 10 hPa) in an electrically-heated high-flux simulator using ceria foams with dual-scale porosity. In the present study, the microstructured ceria foams were subjected to real concentrated high-flux solar radiation in a scalable solar reactor and were found to sustain fuel production cycles without any reactivity

loss. Accordingly, in comparison with previously reported results, a considerable increase in the fuel production rate was achieved with the designed ceria foams exhibiting millimetric cells size and fine granular microstructure within the foam struts.

The studied foams (CF-10 and CF-20) underwent extended cycling during continuous on-sun operation under the various representative conditions reported in Table 1, without suffering any performance decline. Due to the good thermal stability of ceria that can withstand the harsh process conditions, the material performance was not altered during consecutive redox cycles. All the fuel production yields measured for both foams along the cycling experiments are plotted in Figure 10 by highlighting the main parameters influencing the produced fuel amount. The pressure decrease and/or temperature increase during the reduction step both enhance the fuel production yield (>250 µmol/g). Conversely, unfavorable conditions (high oxidation or low reduction temperatures) generally result in the lowest fuel yields (<150 µmol/g). Overall, the two considered cells densities (CF-10 and CF-20) offer very similar fuel production performance at nominal conditions (typically around 200-250 µmol/g). The effect of cell size on temperature distribution and fuel production capacity will be investigated more thoroughly in next studies.

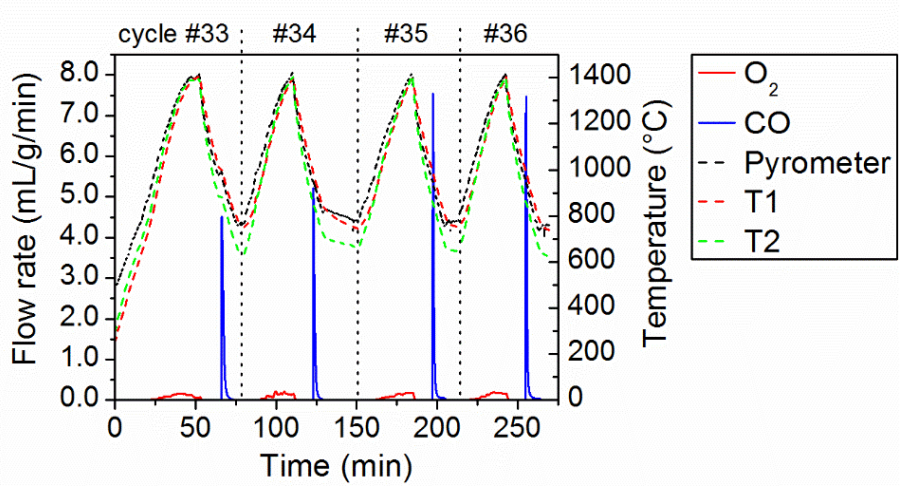

Figure 9: Evolution CO and O_2 production rates with CF-20, during consecutive cycles performed with reduction at 1400°C and 110 hPa, and oxidation during free cooling (CO_2 molar fraction was 0.5 for the two first cycles and 1.0 for the two last ones).

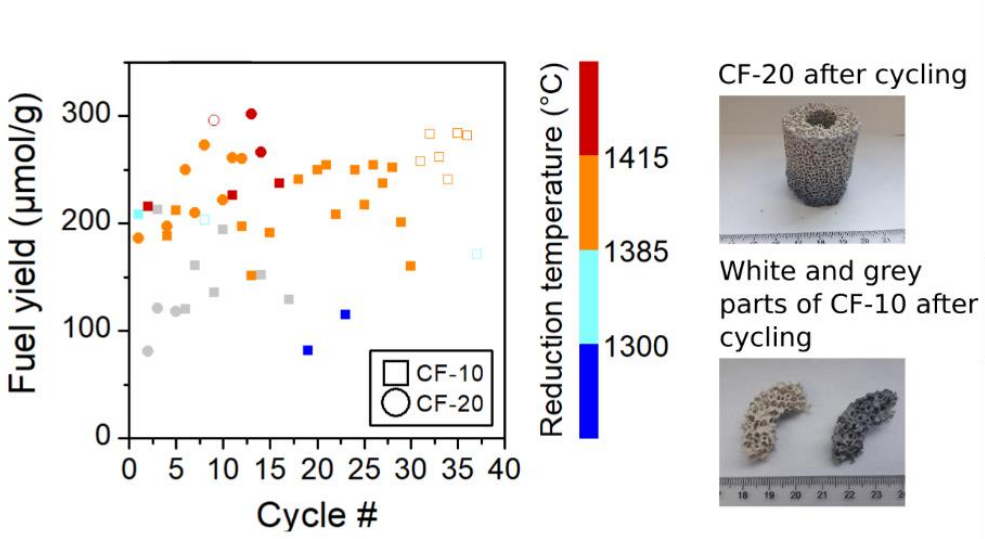

Figure 10: Fuel production yield measured for both foams along the cycling experiments. The symbol color (red to blue) indicates the reduction temperature (T1), emptied interior symbols are related to low pressure during the reduction step, grey symbols are related to unfavorable high oxidation temperatures (T1>1050°C), and symbol shape (square, circle) represents the foam type. (Right: pictures of foams after cycling).

The remarkably high fuel production can be attributed to the monolithic reactor integrating tailored ceria foam morphology and microstructure favoring the oxidation step that is chiefly a surface-controlled reaction [39]. Figure 11a displays a general and cross-section view (Scanning Electron Microscopy – SEM Hitachi S-4800) of CF-10 foam struts before cycling. The grain size, struts porosity, and pore size were estimated by image analysis (ImageJ software). Grain sizes were measured in the range from 3 µm to 10 µm in the fresh sample and micro-scale interconnected porosity within the struts was evidenced (strut porosity: 13%, pore size: 1-5 µm). The presence of hollow struts (cavities in the center of the struts) due to the departure of the organic template during calcination is noticeable, as well as surface cracks (ascribed to degassing during template calcination) which do enhance the available surface area for the oxidation step.

After thermochemical cycling, white or grey zones were observed on the foams (Fig. 10), depending mainly on their position in the reactor cavity (top or bottom part, respectively). SEM micrographs of the white part reveal high densification/sintering but with still remaining residual (closed) porosity (Figure 11b). This densification presumably results from the high temperature occurring in the upper part of the foam, close to the zone receiving highly concentrated solar radiation. Image analysis confirms grain growth (10-40 µm grain size) and struts porosity decrease (7-8% with 3-7 µm pore size). The grey part of the foam is much less densified (Figure 11c) as interconnected macropores in the struts can still be observed (porosity: 10%, pore size: 1-6 µm) and the sizes of grains are similar to those observed

before cycling (3-12 µm). This could also mean that the structure has low thermal conductivity, leading to a lower internal densification as compared to the surface which is exposed to higher fluxes and temperatures. For both parts, the cavities (hollow struts) formed from the removal of the polymer template remain after thermochemical reactions. The cracks observed at the surface of the fresh samples were still observed after the cycles and did not evolve or collapse with time (they were ascribed to the departure of the gaseous species during template calcination/degradation). The presence of both cracks and cavities remaining after cycles suggests a favorable access of the oxidant gas to the reactive ceria grains surface along cycles. The oxidation reaction being surface-controlled [39], a high available geometrical surface and interconnected macroporous network most likely explain the fast oxidation rates obtained with these microstructured ceria foams.

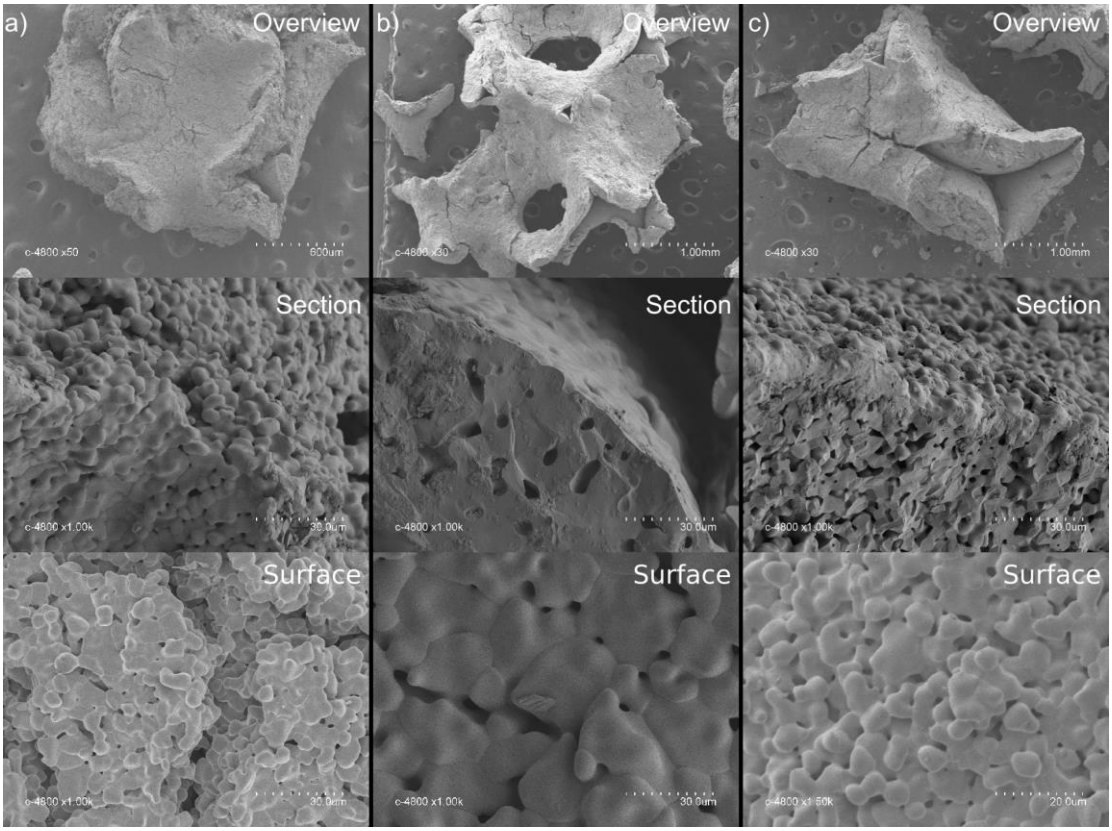

Figure 11: SEM images of CF-10 foam surface and cross-section at different magnifications: a) before cycling, b) white part after cycling, and c) grey part after cycling.

3.4. Energy conversion efficiencies

The solar-to-fuel conversion efficiency is an essential indicator to evaluate the thermochemical process performance. Indeed, thermochemical cycles should reach a solar-

to-fuel conversion efficiency of 20% to be competitive with the combined electrolytic and photovoltaic technologies [40]. The instant solar-to-fuel energy conversion efficiency was calculated according to equation (3),

$$\eta_{solar-to-fuel} = \frac{\dot{n}_{fuel} HHV_{fuel}}{P_{solar}} \quad (3)$$

where $\dot{n}_{fuel}$ is the fuel production rate, HHV_{fuel} the high heating value of the fuel, and P_{solar} the solar power input during the reduction step. For the highest CO production rate (9.93 mL/g/min, cycle #32 of CF-10), the solar-to-fuel conversion efficiency reached ~7.8% (considering maximal power input P_{solar}=1.5 kW, and neglecting the power associated with pumping work and energy penalties arising from inert gas recycling). The order of magnitude of $\eta_{solar\text{-}to\text{-}fuel}$ was then estimated in a more realistic case, accounting for the losses at the aperture and due to the presence of the window, which enhances the calculated efficiency. Taking into account the incident radiation spillage around the cavity aperture due to concentration defects and attenuation by the window due to reflection and absorption (losses amounting to ~10% of P_{solar}), the calculated $\eta_{solar\text{-}to\text{-}fuel}$ rises to 8.6%.

Another conversion efficiency was assessed by considering the cycle energy conversion efficiency not linked to the solar power input but related to the actual mass of cycled ceria, as defined with equation (4),

$$\eta_{cycle} = \frac{n_{fuel} HHV_{fuel}}{\left(\Delta H_{red}(\delta_f) + Cp_{\mathrm{CeO_2}} \Delta T\right) n_{\mathrm{CeO_2}}} \quad (4)$$

where n_{fuel} is the total amount of produced fuel per cycle, $\Delta H_{red}(\delta_f)$ is the reduction enthalpy for the final non-stoichiometry reached (δ_f), $Cp_{\mathrm{CeO_2}}$ is the heat capacity of ceria, ΔT is the temperature swing between the reduction and oxidation steps, and n_{CeO_2} is the quantity of reacting ceria. The ceria heat capacity was taken at 80 J/(mol·K) [41] and the reduction enthalpy at 453 kJ/mol [30]. This efficiency is related to the actual energy consumed by the reaction (ceria heating with ΔT=400°C and reduction enthalpy) and permits to skip the heat losses caused by the small reactor scale. For the cycle #35 of CF-10 (reduction at 1400°C and low pressure), achieving δ=0.049 with a total cycle production of 15.8 mmol of CO (284 µmol/g), η_{cycle} yields 2.9%. Increasing the amount of reacting ceria (using higher density foams with smaller cell sizes) or decreasing the solar power input (by reducing heat losses or improving radiation absorption efficiency of the foam) are possible strategies to improve the solar-to-fuel efficiency. In addition, the above calculated efficiencies should be further enhanced by up-scaling the solar reactor (lower surface-to-volume ratio) and using a sensible heat recovery system. Anyway, it is clear that the solar-to-fuel conversion

efficiencies achieved in this study with reticulated microstructured ceria foams are among the highest obtained to date in a solar-heated reactor.

4. Conclusion

A novel solar reactor was designed and operated for thermochemical splitting of H_2O and CO_2 by two-step redox cycling of microstructured ceria foams. The 10 and 20 ppi open-cell foams underwent 18h and 51h respectively, of on-sun operation without any noticeable performance decline. In total 1.78 NL of H_2 and 11.75 NL of CO were produced by both foams with an average production of 5.1 NmL/g per cycle. An exhaustive investigation of the reactor operational parameters was useful to identify optimal reaction conditions for maximized fuel production. Reactor flexibility was assessed by testing various operating conditions. Robustness in solar processing was demonstrated by operating the system for extended periods at high temperatures under high-flux solar irradiation. During the reduction step, a low pressure (~100 hPa) and a temperature at ~1450°C were found to enhance the reaction extent and associated fuel production yield. The highest non-stoichiometry extent was δ=0.051 at a reduction temperature of 1450°C and atmospheric pressure, which can be further improved by combining also a low reduction pressure (maximum δ=0.060 at 110 hPa). During the oxidation step, both the dynamic temperature regime (free cooling between 1000°C and 800°C) and high oxidant gas concentration resulted in a fast and short duration oxidation step, thus enhancing the fuel production rate. Moreover, the decrease of $CO:CO_2$ ratio also favored the oxidation rate. The fine granular microstructure of the ceria foam (micron-sized grains forming an interconnected macroporous network within the foam struts) remained unchanged after cycling, which is a favorable asset for fast oxidation step. The fuel production rates achieved in the developed solar reactor with reticulated microstructured ceria foams strongly outperformed the previously obtained values (by a factor ~8), and the solar-to-fuel efficiencies (maximum at 8.6%) were also among the highest reported to date for thermochemical cycles performed in a solar reactor. The reactor performance should be further enhanced via scaling-up and optimization of the ceria foam geometry, cell size and macrostructure for maximum solar radiation absorption and uniform heating.

Acknowledgments

This study was supported by the French National Agency for Research (ANR, SUNFUEL project, contract N°ANR-16-CE06-0010). The authors thank R. Garcia (PROMES) for his

technical support during design of the solar reactor, Didier Cot (IEM) for SEM observations and A. Serve (Alsys-CTI) for providing the porous ceria materials.

References

[1] D. Marxer, P. Furler, J. Scheffe, *et al.*, “Demonstration of the Entire Production Chain to Renewable Kerosene via Solar Thermochemical Splitting of H_2O and CO_2,” *Energ. Fuel*, vol. 29, no. 5, pp. 3241–3250, May 2015.

[2] T. Takeshita and K. Yamaji, “Important roles of Fischer–Tropsch synfuels in the global energy future,” *Energy Policy*, vol. 36, no. 8, pp. 2773–2784, Aug. 2008.

[3] T. Montini, M. Melchionna, M. Monai, and P. Fornasiero, “Fundamentals and Catalytic Applications of CeO_2 -Based Materials,” *Chem. Rev.*, vol. 116, no. 10, pp. 5987–6041, May 2016.

[4] A. Haeussler, S. Abanades, J. Jouannaux, M. Drobek, A. Ayral, and A. Julbe, “Recent progress on ceria doping and shaping strategies for solar thermochemical water and CO_2 splitting cycles,” *AIMS Mater. Sci.*, vol. 6, no. 5, pp. 657–684, 2019.

[5] A. Trovarelli, “Catalytic Properties of Ceria and CeO_2 -Containing Materials,” *Catal. Rev.*, vol. 38, no. 4, pp. 439–520, Nov. 1996.

[6] F. A. Costa Oliveira, M. A. Barreiros, S. Abanades, A. P. F. Caetano, R. M. Novais, and R. C. Pullar, “Solar thermochemical CO_2 splitting using cork-templated ceria ecoceramics,” *J. CO_2 Util.*, vol. 26, pp. 552–563, Jul. 2018.

[7] S. Abanades and G. Flamant, “Thermochemical hydrogen production from a two-step solar-driven water-splitting cycle based on cerium oxides,” *Sol. Energy*, vol. 80, no. 12, pp. 1611–1623, Dec. 2006.

[8] M. M. Nair and S. Abanades, “Tailoring Hybrid Nonstoichiometric Ceria Redox Cycle for Combined Solar Methane Reforming and Thermochemical Conversion of H_2O/CO_2,” *Energ. Fuel*, vol. 30, no. 7, pp. 6050–6058, Jul. 2016.

[9] A. Haeussler, S. Abanades, J. Jouannaux, and A. Julbe, “Non-Stoichiometric Redox Active Perovskite Materials for Solar Thermochemical Fuel Production: A Review,” *Catalysts*, vol. 8, no. 12, pp. 611–631, Dec. 2018.

[10] A. Demont, S. Abanades, and E. Beche, “Investigation of Perovskite Structures as Oxygen-Exchange Redox Materials for Hydrogen Production from Thermochemical Two-Step Water-Splitting Cycles,” *J. Phys. Chem. C*, vol. 118, no. 24, pp. 12682–12692, Jun. 2014.

[11] M. M. Nair and S. Abanades, “Insights into the Redox Performance of Non-stoichiometric Lanthanum Manganite Perovskites for Solar Thermochemical CO_2 Splitting,” *ChemistrySelect*, vol. 1, no. 15, pp. 4449–4457, Sep. 2016.

[12] A. H. McDaniel, E. C. Miller, D. Arifin, *et al.*, “Sr- and Mn-doped $LaAlO_{3-\delta}$ for solar thermochemical H_2 and CO production,” *Energ. Environ. Sci.*, vol. 6, no. 8, pp. 2424–2428, 2013.

[13] J. R. Scheffe, D. Weibel, and A. Steinfeld, “Lanthanum–Strontium–Manganese perovskites as redox materials for solar thermochemical splitting of H_2O and CO_2,” *Energ. Fuel*, vol. 27, no. 8, pp. 4250–4257, Aug. 2013.

[14] T. Cooper, J. R. Scheffe, M. E. Galvez, R. Jacot, G. Patzke, and A. Steinfeld, “Lanthanum Manganite Perovskites with Ca/Sr A-site and Al B-site Doping as Effective Oxygen Exchange Materials for Solar Thermochemical Fuel Production,” *Energy Technol.*, vol. 3, no. 11, pp. 1130–1142, Nov. 2015.

[15] J. E. Miller, A. Ambrosini, E. N. Coker, M. D. Allendorf, and A. H. McDaniel, “Advancing Oxide Materials for Thermochemical Production of Solar Fuels,” *Energy Procedia*, vol. 49, pp. 2019–2026, 2014.

[16] M. E. Gálvez, R. Jacot, J. Scheffe, T. Cooper, G. Patzke, and A. Steinfeld, “Physico-chemical changes in Ca, Sr and Al-doped La–Mn–O perovskites upon thermochemical splitting of CO_2 via redox cycling,” *Phys. Chem. Chem. Phys.*, vol. 17, no. 9, pp. 6629–6634, 2015.

[17] Y. Hao and A. Steinfeld, “Fuels from water, CO_2 and solar energy,” *Sci. Bull.*, vol. 62, no. 16, pp. 1099–1101, Aug. 2017.

[18] H. S. Cho, N. Gokon, T. Kodama, Y. H. Kang, and H. J. Lee, “Improved operation of solar reactor for two-step water-splitting H_2 production by ceria-coated ceramic foam device,” *Int. J. Hydrogen Energy*, vol. 40, no. 1, pp. 114–124, Jan. 2015.

[19] H. S. Cho, T. Myojin, S. Kawakami, *et al.*, “Solar Demonstration of Thermochemical Two-step Water Splitting Cycle Using CeO_2/MPSZ Ceramic foam Device by $45kW_{th}$ KIER Solar Furnace,” *Energy Procedia*, vol. 49, pp. 1922–1931, 2014.

[20] B. J. Hathaway, R. Bala Chandran, A. C. Gladen, T. R. Chase, and J. H. Davidson, “Demonstration of a Solar Reactor for Carbon Dioxide Splitting via the Isothermal Ceria Redox Cycle and Practical Implications,” *Energ. Fuel*, vol. 30, no. 8, pp. 6654–6661, Aug. 2016.

[21] W. C. Chueh, C. Falter, M. Abbott, *et al.*, “High-Flux Solar-Driven Thermochemical Dissociation of CO_2 and H_2O Using Nonstoichiometric Ceria,” *Science*, vol. 330, no. 6012, pp. 1797–1801, Dec. 2010.

[22] P. Furler, J. Scheffe, M. Gorbar, L. Moes, U. Vogt, and A. Steinfeld, “Solar Thermochemical CO_2 Splitting Utilizing a Reticulated Porous Ceria Redox System,” *Energ. Fuel*, vol. 26, no. 11, pp. 7051–7059, Nov. 2012.

[23] P. Furler, D. Marxer, J. Scheffe, *et al.*, “Solar kerosene from H_2O and CO_2,” *AIP Conference Proceedings*, vol. 1850, no. 1, p. 100006, Jun. 2017.

[24] D. Marxer, P. Furler, M. Takacs, and A. Steinfeld, “Solar thermochemical splitting of CO_2 into separate streams of CO and O_2 with high selectivity, stability, conversion, and efficiency,” *Energ. Environ. Sci.*, vol. 10, no. 5, pp. 1142–1149, 2017.

[25] R. B. Diver, J. E. Miller, N. P. Siegel, and T. A. Moss, “Testing of a CR5 Solar Thermochemical Heat Engine Prototype,” in *ASME 2010 4th International Conference on Energy Sustainability, Volume 2*, Phoenix, Arizona, USA, 2010, pp. 97–104.

[26] J. E. Miller, M. D. Allendorf, A. Ambrosini, *et al.*, “Reimagining Liquid Transportation Fuels: Sunshine to Petrol,” Sandia National Laboratories, USA, SAND2012-0307, 2012.

[27] H. I. Villafán-Vidales, C. A. Arancibia-Bulnes, D. Riveros-Rosas, H. Romero-Paredes, and C. A. Estrada, “An overview of the solar thermochemical processes for hydrogen and syngas production: Reactors, and facilities,” *Renew. Sustain. Energ. Rev.*, vol. 75, pp. 894–908, Aug. 2017.

[28] S. Karl and A. V. Somers, “Method of making porous ceramic articles,” United States, US3090094A, 21-May-1963.

[29] J. R. Scheffe and A. Steinfeld, “Thermodynamic Analysis of Cerium-Based Oxides for Solar Thermochemical Fuel Production,” *Energ. Fuel*, vol. 26, no. 3, pp. 1928–1936, Mar. 2012.

[30] R. J. Panlener, R. N. Blumenthal, and J. E. Garnier, “A thermodynamic study of nonstoichiometric cerium dioxide,” *J. Phys. Chem. Solids*, vol. 36, no. 11, pp. 1213–1222, Nov. 1975.

[31] S. Ackermann, L. Sauvin, R. Castiglioni, J.L.M. Rupp, J.R. Scheffe, and A. Steinfeld, “Kinetics of CO_2 Reduction over Nonstoichiometric Ceria”, *J. Phys. Chem. C*, 119, 29, 16452-16461, 2015.

[32] P. Furler, D. Marxer, M. Takacs, and A. Steinfeld, “Solar thermochemical reactor technology for splitting CO_2,” *AIP Conference Proceedings*, vol. 2033, no. 1, p. 130005, Nov. 2018.

[33] H. Kong, X. Kong, H. Wang, J. Wang, “A strategy for optimizing efficiencies of solar thermochemical fuel production based on nonstoichiometric oxides”, *Int. J. Hydrogen Energy*, vol. 44, issue 36, pp. 19585-19594, Jul. 2019.

[34] R.J. Carrillo and J.R. Scheffe, “Beyond Ceria: Theoretical Investigation of Isothermal and Near-Isothermal Redox Cycling of Perovskites for Solar Thermochemical Fuel Production”, *Energy Fuels*, vol. 33, no. 12, pp. 12871-12884, 2019.

[35] R. Bader, L. J. Venstrom, J. H. Davidson and W. Lipiński, “Thermodynamic Analysis of Isothermal Redox Cycling of Ceria for Solar Fuel Production”, *Energy Fuels*, 27, 9, pp. 5533-5544, 2013.

[36] B. Bulfin, F. Call, M. Lange, O. Lübben, C. Sattler, R. Pitz-Paal, and I. V. Shvets, “Thermodynamics of CeO_2 Thermochemical Fuel Production”, *Energy Fuels*, 29, 2, pp. 1001-1009, 2015.

[37] A. de la Calle, A. Bayon, “Annual performance of a thermochemical solar syngas production plant based on non-stoichiometric CeO_2”, *Int. J. Hydrogen Energy,* Vol. 44, Issue 3, pp. 1409-1424, Jan. 2019.

[38] B.D. Ehrhart, C.L. Muhich, I. Al-Shankiti A.W. Weimer, “System efficiency for two-step metal oxide solar thermochemical hydrogen production – Part 2: Impact of gas heat recuperation and separation temperatures”, *Int. J. Hydrogen Energy,* vol. 41, Issue 44, pp. 19894-19903, Nov. 2016.

[39] W. C. Chueh and S. M. Haile, “A thermochemical study of ceria: exploiting an old material for new modes of energy conversion and CO_2 mitigation,” *Phil. Trans. R. Soc. A*, vol. 368, no. 1923, pp. 3269–3294, Jul. 2010.

[40] N. P. Siegel, J. E. Miller, I. Ermanoski, R. B. Diver, and E. B. Stechel, “Factors Affecting the Efficiency of Solar Driven Metal Oxide Thermochemical Cycles,” *Ind. Eng. Chem. Res.*, vol. 52, no. 9, pp. 3276–3286, Mar. 2013.

[41] M. Ricken, J. Nölting, and I. Riess, “Specific heat and phase diagram of nonstoichiometric ceria (CeO_{2-x}),” *J. Solid State Chem.*, vol. 54, no. 1, pp. 89–99, Aug. 1984.